https://doi.org/10.1038/s44453-026-00038-9

Subsurface ice in doubly shadowed craters as revealed by Chandrayaan-2 dual frequency synthetic aperture radar

Rishitosh K. Sinha ✉, Rajiv R. Bharti, Kinsuk Acharyya, Sanjay K. Mishra, Neeraj Srivastava & Anil Bhardwaj

Doubly shadowed craters at the lunar poles provide ideal environments for preserving subsurface ice. Located within permanently shadowed regions, their raised rims additionally block scattered light and thermal emission from nearby illuminated surfaces, allowing crater interior temperatures to reach around 25 K. Using full-polarimetric L- and S-band observations from Chandrayaan-2's Dual Frequency Synthetic Aperture Radar, we investigate the presence of subsurface ice in nine doubly shadowed craters located within Faustini, Haworth, and Shoemaker craters. Four craters exhibit circular polarization ratio values greater than 1 together with low degrees of polarization (<0.13), allowing us to establish a refined diagnostic criterion for identifying subsurface ice through volumetric scattering. A ~ 1.1 km wide crater within Faustini shows enhanced radar polarization and a prominent lobate-rim morphology, indicating potential excavation into subsurface ice. These observations provide strong evidence for subsurface ice in doubly shadowed craters and support long-term volatile retention processes at the lunar poles.

Investigating the distribution and stability of water-ice at the lunar poles has long been a key scientific priority[1–13], particularly for assessing in situ resources essential for supporting future crewed lunar missions and outposts[14–16]. Among the coldest environments on the Moon[1–13], doubly shadowed craters represent a special class of craters located within larger permanently shadowed regions at the lunar poles[17–19]. The raised rim of the doubly shadowed crater provides effective double shielding of the crater interior from scattered light and thermal emission from nearby sunlit surfaces[17–19]. Because of this double shielding, thermal modeling predicts that the floors of these craters can reach extremely low temperatures of ~25 K[17–19] and are thus high priority targets for hosting stable subsurface water-ice deposits in their interior[18].

Over the past two decades, a suite of lunar missions equipped with state-of-the-art instruments has progressively suggested surface and subsurface water-ice at the lunar poles[3,4,6–12]. The Moon's small axial tilt (~ 1.5°) limits solar illumination in topographic depressions[19–21], creating permanently shadowed regions within craters poleward of 80° [22]. In the absence of direct sunlight, the temperatures within permanently shadowed regions can fall below ~110 K[22–24], a threshold below which water-ice can remain stable against sublimation over geological timescales[8,25,26]. The rates of sublimation decreases exponentially with decreasing temperature, such that water-ice can become increasingly stable at lower temperatures and persist over geological timescales[8]. However, the long-term stability of water-ice would also depend upon the interplay between sublimation rates, delivery mechanisms, and regolith mixing processes[8]. Potential water sources include exogenic delivery by volatile-rich impactors[25,26], endogenic contributions from volcanic outgassing[27], and in situ production via regolith-solar wind interactions[2]. A wide range of remote sensing measurements using neutron spectroscopy[3], ultraviolet imaging and near-infrared spectroscopy[6,8,11], thermal infrared radiometry[24], and lidar reflectometry[9,28,29] have supported the view of surface/subsurface water-ice presence in permanently shadowed regions. The in situ evidence of water-ice within a permanently shadowed portion inside Cabeus crater by the Lunar Crater Observation and Sensing Satellite (LCROSS) mission substantiated the remote sensing claims[30,31].

Water-ice within permanently shadowed regions has been investigated using radar observations from both Earth-based instruments and spacecraft orbiting the Moon[7,32–37]. A commonly used radar signature is the Circular Polarization Ratio (CPR), defined as the ratio of radar echoes with the same circular polarization as the transmitted signal to those with the opposite polarization[12,36], is used to determine the presence of water-ice. Water-ice typically produces CPR > 1 because radar waves can scatter multiple times within an ice-rich medium[38–41], while dry regolith has CPR < 1[36,39]. Radar observations from instrument such as the Mini-RF on the Lunar Reconnaissance Orbiter[7,36], together with radar scattering models[42] and datasets from other instruments[3–12], have identified elevated CPR in many

Physical Research Laboratory, Ahmedabad, India. ✉e-mail: rishitosh@prl.res.in

permanently shadowed craters[7]. Additional observations combining Mini-RF instrument measurements with radar data from the Arecibo Observatory also reported presence of near surface water-ice in several polar craters[37]. Likewise, the Mini Synthetic Aperture Radar instrument on Chandrayaan-1 reported water-ice signatures in 34 permanently shadowed craters near the lunar North Pole[36]. However, interpretations of radar-based water-ice signatures have often been regarded as ambiguous[43]. High CPR can also arise from rough, blocky surfaces where radar waves undergo multiple double-bounce reflections[43]. For instance, Mini-RF radar observations of the Shackleton crater revealed high CPR along its rough inner walls, while its floor showed lower CPR values[33]. Such a change in CPR ruled out presence of surficial water-ice and suggested linkages with surface roughness[33].

The arrival of Chandrayaan-2 in the lunar orbit provided a new opportunity to address these ambiguities using observations from its Dual Frequency Synthetic Aperture Radar instrument[12]. This radar operates at two wavelengths (L-band and S-band) and provides relatively higher spatial resolution (2–75 m per pixel) than earlier lunar radar instruments. It also records multiple polarization modes (HH, HV, VV, and VH polarization combinations) of the reflected radar signal[12], enabling a more detailed characterization of scattering mechanisms[44]. However, analysis of radar observations from 115 polar craters revealed insignificant presence of water-ice mixed within the regolith[12]. Nevertheless, some craters did show enhanced CPR suggesting the presence of water-ice, for instance, $a \sim 3.5$ km crater on the rim of Faustini crater[12]. However, it was not sure whether the observed radar signatures were truly caused by water-ice, mainly because the locations of radar signals did not coincide with predicted cold trap areas[45].

A key insight from radar and illumination modeling studies is that the areas with elevated CPR within permanently shadowed regions are not always dark[17]. Although these areas do not receive direct solar illumination, they can still be exposed to scattered sunlight and thermal emission from nearby illuminated surfaces[17]. In contrast, the interior of the doubly shadowed craters located within these permanently shadowed regions are double shielded from scattered light and thermal emission from nearby sunlit surfaces[17,18]. Doubly shadowed craters have been identified within the permanently shadowed floors of Haworth (~ 51 km diameter), Shoemaker (~ 52 km diameter), and Faustini (41 km diameter) craters near the lunar South Pole[17] (Fig. 1). Among these host craters, Faustini holds the largest percentage of total doubly shadowed area (0.564 km^2), followed by Shoemaker (0.446 km^2) and Haworth (0.308 km^2)[17]. Previously, four doubly shadowed craters have been mapped within Faustini, and three each within Shoemaker and Haworth[17]. In this study, we analyze the radar observations of the interior

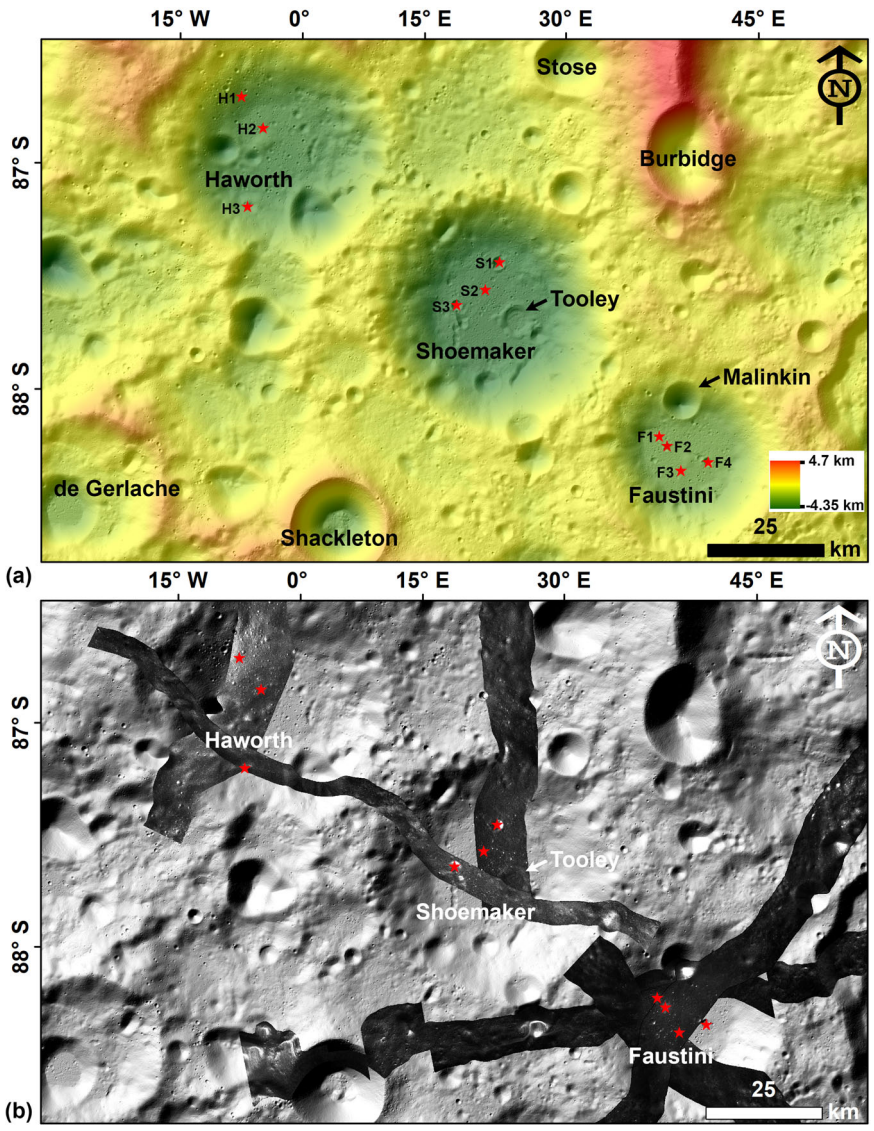

Fig. 1 | Locations of doubly shadowed craters investigated in this study. a Lunar Reconnaissance Orbiter Wide Angle Camera mosaic of the south polar region of the Moon. The mosaic is overlaid on the 10 m/pixel Digital Elevation Model (DEM) of the South Pole from Lunar Orbiter Laser Altimeter[56]. **b** Dual Frequency Synthetic Aperture Radar coverage of doubly shadowed craters within Faustini, Shoemaker and Haworth crater. The radar datasets are overlaid on LOLA DEM-based hillshade image of the South Polar Region. In **a**, **b**, the locations of doubly shadowed craters are shown by red star symbols. Tooley crater within Shoemaker is marked by an arrow in **a**, **b**. Additionally, in **a** the craters located within Faustini are shown as F1, F2, F3, and F4; Shoemaker as S1, S2, and S3; Haworth as H1, H2, and H3. The list of Dual Frequency Synthetic Aperture Radar datasets used in this study is provided in Supplementary Table 1.

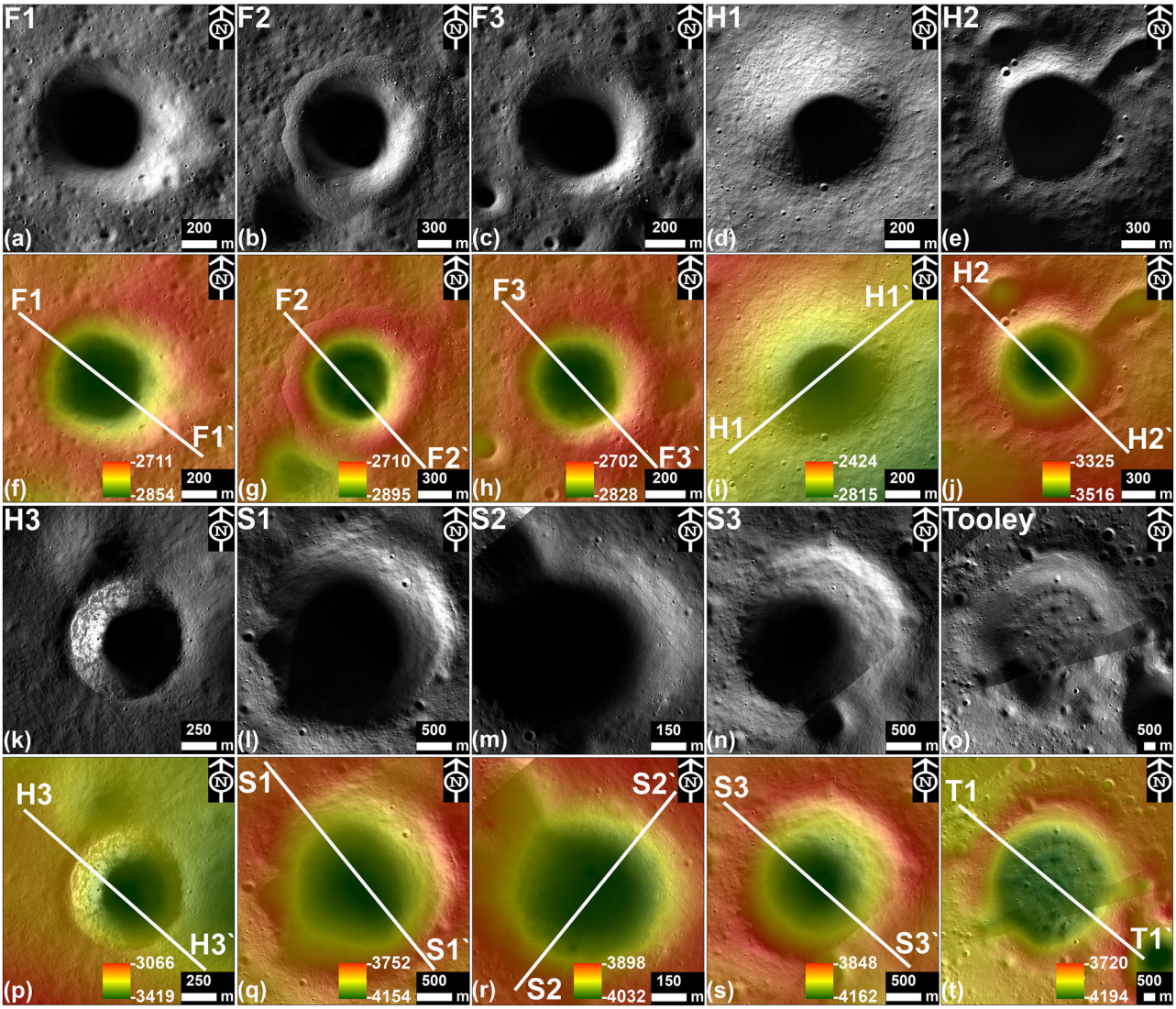

Fig. 2 | Morphology and topography of craters investigated in this study. ShadowCam images (**a**–**e**, **k**–**n**) and corresponding LOLA DEMs (**f**–**j**, **p**–**s**) overlaid on ShadowCam images of the doubly shadowed craters investigated in this study. Tooley crater ShadowCam image and LOLA DEM are shown in **o**, **t** respectively. Note that the interior of all the craters located within permanently shadowed regions are marked by shadow. The transects (solid white lines) overlaid on the DEMs are topographic profiles of the craters shown in Supplementary Fig. 2.

of these doubly shadowed craters to infer about the presence of subsurface ice. Moreover, we have conducted a detailed comparative analysis of the morphology, topography, and radar characteristics of the doubly shadowed craters to constrain the possible existence of water-ice deposits in the lunar South Polar Region. Radar data are unavailable for one of the doubly shadowed craters (crater F4) in the Faustini crater, limiting us to assess its subsurface ice containing potential. Therefore, we focus on nine doubly shadowed craters in this work. Our analysis aims at refining the interpretation of radar signatures in the context of lunar subsurface ice detection.

ShadowCam images reveal the presence of boulders along the rims and walls of most of the doubly shadowed craters, except crater H1 (Fig. 2; Table 1). Boulders are also present around these craters within approximately one crater radii. However, the floors of these craters, which are doubly shadowed, contain relatively lesser number of boulders (Supplementary Fig. 1). The doubly shadowed craters range in diameter from small (700–1200 m) to large (2500–3000 m) (Table 1). Among the smaller craters, F2, F3, H1 and H3 (diameter range: 700 to 1100 m) exhibit relatively steep walls (18° to 29°), whereas the remaining craters have gentler slopes (< 18°) (Table 1; Supplementary Fig. 2). Crater F2 has been previously identified as a well-defined lobate-rim crater[46,47], and thermal models suggest interior temperatures ≤55 K[17,48]. This lobate-rim morphology has been interpreted as evidence that the crater formed in a target containing subsurface ice[46]. Crater F3 shows evidence of partial lobate-rim around its southeastern to southwestern rim and a raised eastern rim (Fig. 1 and Supplementary Fig. 2), which potentially shields the crater interior from scattered light and thermal emission from nearby sunlit surfaces, allowing temperatures to remain below 100 K[48]. In contrast, crater H3 lacks a lobate-rim but its exterior is surrounded by extensive impact melt flows extending up to 3–5 crater radii from its rim (Supplementary Fig. 3). The remaining small doubly shadowed craters (F1, S2, H1 and H2) display ordinary morphological characteristics (Fig. 2). There are two large doubly shadowed craters (S1 and S3) on the floor of Shoemaker that lack pronounced boulder concentrations and exhibit gentler wall slopes (13–16°), suggesting that these craters are likely older than the smaller doubly shadowed craters (Fig. 2; Table 1). To further probe into possible presence of subsurface ice, we also examined Tooley crater (~ 7000 m diameter) on the floor of Shoemaker crater that displays a partial lobate-rim morphology (Figs. 1 and 2j). Tooley crater exhibits a low depth-to-diameter ratio (0.039–0.048), gentle wall slopes (< 10°), and minor boulder presence (Table 1), all of which suggest Tooley to be older than the

Table 1 | Location, diameter, depth, wall slope, and morphological characteristics of the doubly shadowed craters investigated in this study

Craters	Latitude	Longitude	Diameter (m)	Depth (m)	d/D	Raised rim	CW slope (degrees)	Boulder presence	Lobate rim
F1	−87.436	80.655	950	119–122	0.125–0.128	Yes	16.5–17	Moderate	No
F2	−87.39	82.31	1100	137–151	0.124–0.137	Yes	20–27	Major	Yes
F3	−87.31	86.333	700	88–103	0.125–0.147	Yes	18–20	Major	No
S1	−87.841	40.078	2980	337–353	0.113–0.118	Yes	13–16	Moderate	No
S2	−88.049	41.71	1060	93–101	0.087–0.095	Yes	15–18	Moderate	No
S3	−88.275	38.992	2580	254–287	0.098–0.111	Yes	14–15.5	Moderate	No
H1	−87.138	351.335	1060	90–140	0.084–0.132	Yes	18–20	No	No
H2	−87.381	353.895	1170	140–150	0.119–0.128	Yes	17.5–18	Minor	No
H3	−87.915	349.058	800	140–201	0.175–0.251	Yes	24.3–28.9	Major	No
Tooley	−88.04	51.05	7050	280–340	0.039–0.048	Yes	7.7–9.3	Minor	Yes (partial)

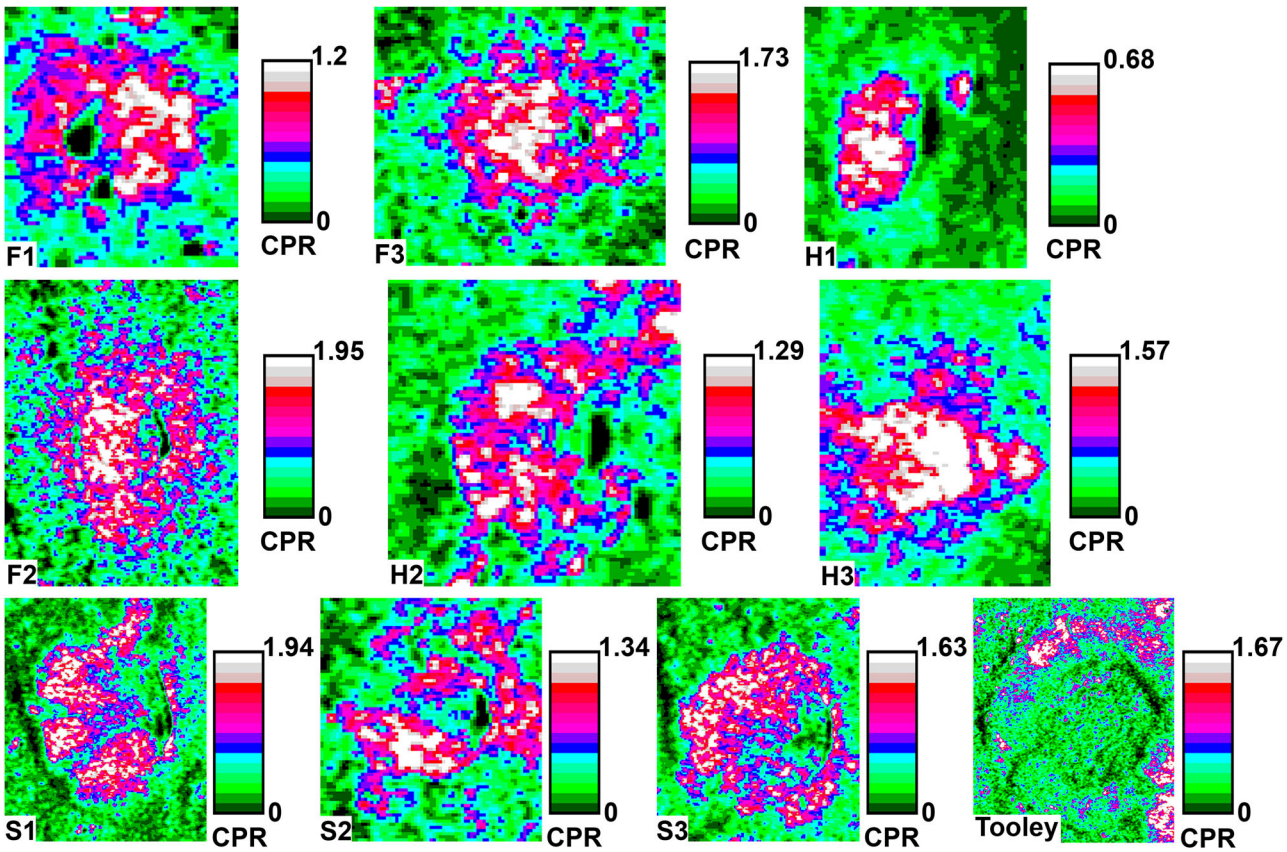

Fig. 3 | Circular Polarization Ratio of craters investigated in this study. Dual Frequency Synthetic Aperture Radar-based Circular Polarization Ratio (CPR) of the interior of doubly shadowed craters investigated in this study. All the craters are marked by their corresponding names, as shown in Fig. 1. CPR of the interior of Tooley crater is also shown. The locations of the region of interest for which CPR has been estimated are shown in Supplementary Fig. 4.

doubly shadowed craters. Although crater Tooley is not itself doubly shadowed, previous studies have proposed its formation may have involved ice-rich material in the target[49].

Results

Radar signatures of doubly shadowed craters

Radar observations from the Dual frequency Synthetic Aperture Radar on Chandrayaan-2 show elevated CPR values (>1) within the interiors of four doubly shadowed craters: F2, F3, H3, and S1 (Fig. 3 and Supplementary Fig. 4). Craters F2 and F3 contains the highest fractions of CPR elevated pixels, comprising about 47% and 42% of their interiors, respectively (Supplementary Fig. 5). In comparison, craters H3 and S1 show elevated CPR in only around 10% and 8% of interior pixels (Supplementary Fig. 5). Among these craters, the highest CPR measured is 1.95 in crater F2, followed by 1.94 in S1, 1.73 in F3 and 1.57 in H3 (Fig. 3). Although crater S1 reaches a value comparable to F2, the number of CPR elevated pixels in F2 is six times higher (Supplementary Fig. 5). Four additional craters (F1, H2, S2, and S3) contain fewer than 3% of interior pixels with elevated CPR values and were therefore excluded from further analysis (Supplementary Fig. 5). Crater H1 and Tooley show no evidence of elevated CPR within their interiors (Figs. 3 and 4).

Previous studies have noted that elevated CPR found in the interior of young craters does not necessarily indicate subsurface ice[43], because elevated CPR can also arise from rough surfaces containing pronounced number of

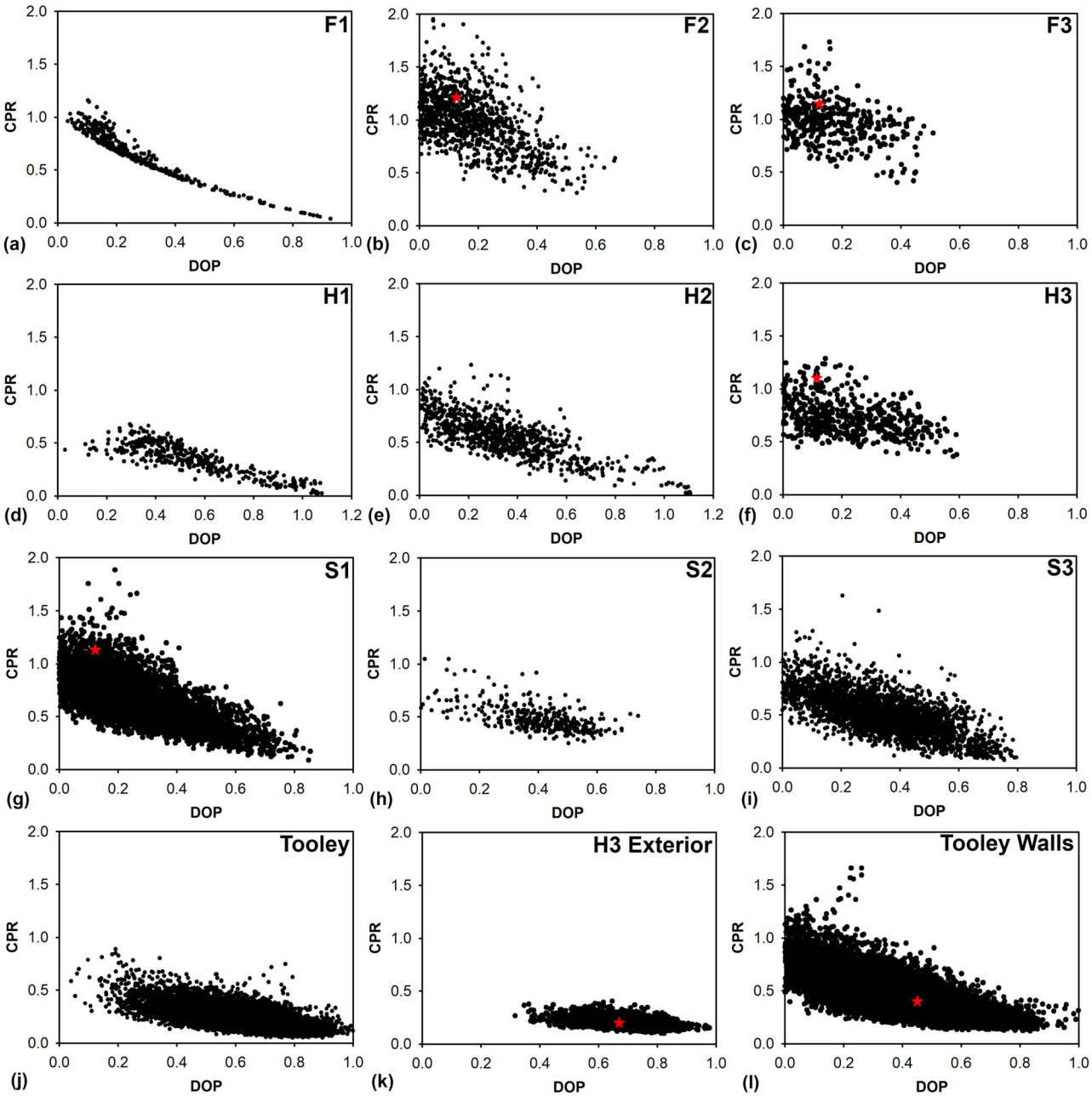

Fig. 4 | Relationship between Circular Polarization Ratio (CPR) and Degree of Polarization (DOP) of investigated craters. a–i The interior of the nine doubly shadowed craters, **j** Tooley floor, **k** H3 exterior, and l Tooley walls. The locations of the region of interest for which CPR and DOP have been derived are shown in Supplementary Fig. 4. Red star symbol in **b**, **c**, **f**, **g** shows the average CPR and DOP of pixels having CPR 1. In **k**, **l** the red star symbol shows the average CPR and DOP of the entire data shown in the plot.

rocks[7,33,36,43,50]. The young craters have been interpreted to represent an intermediate stage in typical crater degradation and evolution[43]. To address this apparent controversy, we also quantified the degree of radar signal polarization by estimating DOP[51]. Previous studies have shown that for a given crater, the combination of CPR > 1 and DOP < 0.35 provides convincing evidence of volume scattering, which is consistent with the presence of subsurface ice[45,51]. However, it is important to note that lower values of DOP (i.e., approaching 0) suggest stronger depolarization of the radar signal, which is typical of volumetric scattering[51]. Our analysis shows that areas with elevated CPR consistently show low average DOP values, ranging from 0.1 to 0.13 in craters F2, F3, H3, and S1 (Fig. 4). These values are significantly lower than previously proposed thresholds (Fig. 4). Based on this relationship, we refine the radar diagnostic criterion for identifying volumetric scattering, showing that CPR > 1 combined with DOP < 0.13 provides a strong indicator of subsurface ice. In contrast, crater H1 and Tooley crater exhibit much higher average DOP value of 0.55 and 0.66, respectively (Fig. 4), without elevated CPR pixels.

Refining the radar criterion for subsurface ice

We further evaluated the refined criterion for identifying volumetric scattering across the studied doubly shadowed craters. In all craters showing potential evidence of volumetric scattering, regions with average CPR values below 1 show average DOP between 0.2 and 0.3 (Fig. 4). Around crater F2, where rough surfaces dominate the regions outside the crater, it can be seen that regions with average CPR of 1.1 correspond to an average DOP of 0.17 (Supplementary Fig. 6). Although this occurs in less than 2% pixels. In

contrast, regions where average CPR value drops below 1, the average DOP increases substantially to 0.48 (Supplementary Fig. 6). Similarly, in the exterior region of crater H3, regions associated with impact melt flows show average DOP as high as 0.67 when average CPR drops below 1 (Fig. 4k and Supplementary Fig. 4). A comparable pattern is observed in Tooley crater, which has less than 1% of elevated CPR pixels on its walls. In this region, the average CPR is 0.4 and DOP is 0.45 (Fig. 4l). Collectively, these results indicate that in regions where volumetric scattering is not anticipated, such as crater rims, walls, and ejecta consistently show high DOP values. Further, even if the with average CPR value exceeds 1, the average DOP value remains above the refined threshold of 0.13. Moreover, when average CPR drops below 1, the average DOP typically exceeds further, reaching values between 0.2 and 0.67. These observations further support the correlation of low DOP (< 0.13) combined with CPR values (>1) as criterion for identifying volumetric scattering associated with subsurface ice. It is important to note that the combined absence of elevated CPR and low DOP in some doubly shadowed craters investigated in this study does not necessarily imply complete absence of subsurface ice. The radar observations are sensitive mainly to the upper subsurface layer[12]. If ice deposits occur at depths greater than the penetration depth of the radar signal (few meters)[12], they may remain undetected in the present analysis.

Discussions

Previous studies have suggested that small (400–1000 m) simple craters formed in targets containing subsurface ice often have depth-to-diameter ratios of around 0.16–0.21[52,53]. The presence of ice makes the subsurface harder surface than the loose regolith, thereby causing a lower depth-to-diameter ratio[52]. Among the doubly shadowed craters examined in this study, depth-to-diameter ratio of all the small craters exhibits a ratio lower than 0.16 (Table 1), though not all show elevated CPR values within their interiors. Moreover, craters that display elevated CPR and low DOP relationships, such as H3, have depth-to-diameter ratios greater than 0.16 (Table 1; Fig. 4). In contrast, Tooley crater exhibits the lowest depth-to-diameter ratios but no evidence of elevated CPR pixels within their interiors (Table 1; Fig. 4). Therefore, we do not consider depth-to-diameter ratio alone to be a reliable indicator of subsurface ice. This inference is consistent with previous studies suggesting that subsurface ice is unlikely to be the major driver of reduced crater depth[53]. Nonetheless, the subsurface ice may still alter crater morphology, particularly if the impact penetrates the subsurface ice.

The distinctive lobate-rim morphology of crater F2 provides independent evidence supporting the hypothesis that the target material at the impact site may have contained subsurface ice (Fig. 5a). On the floor of Faustini crater, the impact point of crater F2 is located at an elevation of −2744 m (Fig. 5b), whereas the elevation of surrounding crater floor ranges from −2560 m to −2755 m (Fig. 5b). This means that the impact occurred ~180 m below the surrounding permanently shadowed floor of Faustini. Furthermore, the floor of crater F2 itself lies at an elevation of -2860 m (Fig. 5c), which is approximately 300 m beneath the upper surface of the Faustini floor. Such a deep impact event within Faustini may have penetrated subsurface ice, producing the observed lobate-rim morphology (Fig. 5c). Although some lunar polar craters exhibit partial lobate-rim looking morphology, none is as prominent as the lobate-rimmed crater F2 discussed in this study, indicating a heterogeneous distribution of subsurface ice in both depth and spatial extent. It is important to mention here that the absence of prominent lobate-rim morphology in other doubly shadowed craters does not necessarily rule out the presence of subsurface ice. If the subsurface ice resides at a depth deeper than the penetration depth of the impact, the resulting crater may not possess a pronounced lobate-rim morphology even if subsurface ice is present. Moreover, we emphasize that our analysis is limited to a selected set of lunar impact craters defined by a specific range of diameters and morphological characteristics. Therefore, caution should be exercised when extrapolating these inferences to broader contexts.

Further investigation of doubly shadowed craters with partial lobate-rim morphologies confirms that, except for crater F2, none formed within the lowest unit of the host crater floor (Supplementary Fig. 7 and 8). Further, the raised rim of crater F2, about 20–25 m high, helps in effective shielding of its interior from scattered light and thermal emission from surrounding surfaces. This shielding helps in maintaining persistently low annual

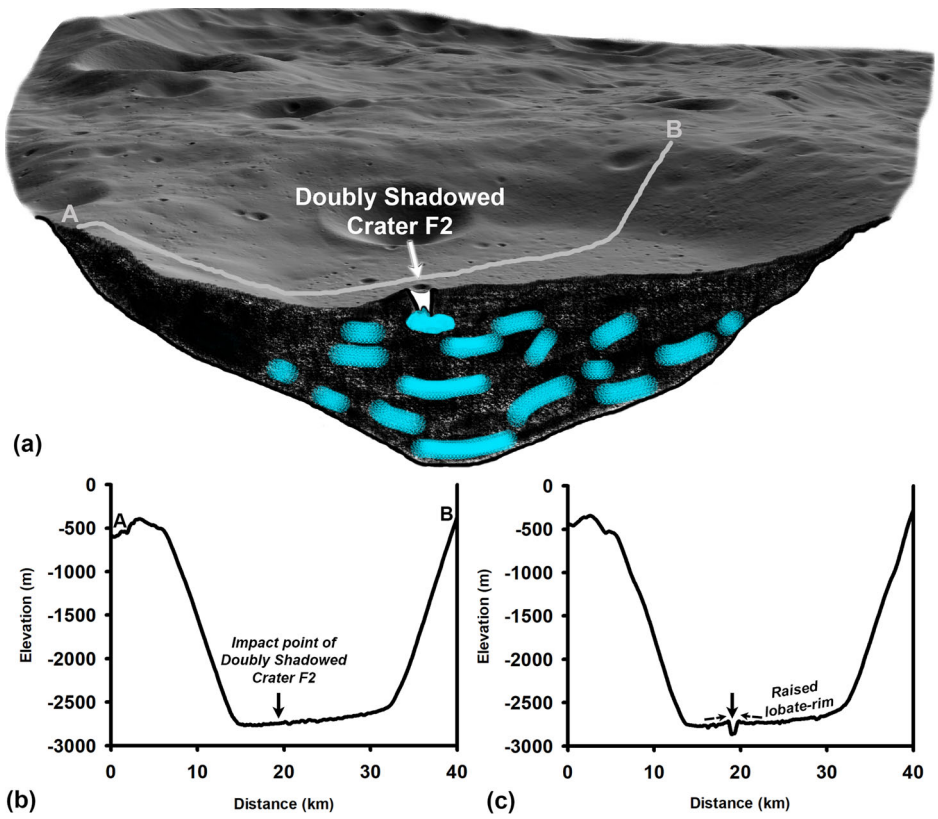

Fig. 5 | Formation of a doubly shadowed crater with a prominent lobate-rim within Faustini permanently shadowed region. a A conceptual sketch illustrating the probable scenario for the formation of doubly shadowed crater F2 with a prominent lobate-rim. The impact point of crater F2 in the Faustini permanently shadowed region is located within the lower unit at an elevation of -2744 m, which is located around 180 m below the top unit of the crater floor, as shown in **b**. At such a lower depth within Faustini permanently shadowed region, an impact is likely to penetrate the subsurface ice located at a shallower depth. The penetration into the subsurface ice resulted in the emplacement of a prominent raised lobate-rim around the crater, as shown in **c**. The image showing the permanently shadowed region floor and the surrounding regions of Faustini is generated from the hillshade of the South Pole DEM. In the sketch, the subsurface inside the Faustini permanently shadowed region is shown in shades of gray and black, and subsurface ice is shown in cyan. Note that the layers shown in the sketch are not to scale.

Table 2 | Radar signatures and inferred subsurface ice presence in doubly shadowed craters

Crater	Host crater	CPR > 1	DOP < 0.13	Presence of subsurface ice
F2	Faustini	Yes	Yes	Strong evidence
F3	Faustini	Yes	Yes	Likely
H3	Haworth	Partial	Partial	Partially likely
S1	Shoemaker	Partial	Partial	Partially likely
F1	Faustini	No	No	No evidence
H1	Haworth	No	No	No evidence
H2	Haworth	No	No	No evidence
S2	Shoemaker	No	No	No evidence
S3	Shoemaker	No	No	No evidence
Tooley	Shoemaker	No	No	No evidence

minimum temperatures and promotes retention of volatiles over geological timescales. Overall, these observations make it very likely that the impact site of crater F2 likely contained subsurface ice inside Faustini permanently shadowed region, which might persist beneath its floor even today. The possibility of geologically recent volatile emplacement in the lunar polar regions also remains[53], which might explain the radar signatures in other craters (F3, H3 and S1) that lack typical lobate-rim morphology. While the studied craters lie within permanently shadowed regions, temperature dependent sublimation rates remain low[46–48], thereby providing a compelling case for cold trapping and retention of volatiles over geological timescales. This assumption of post deposition volatile delivery might occur throughout permanently shadowed regions, but long-term retention appears to be most effective in doubly shadowed craters where thermal shielding is strongest[44,45,48].

Analysis of nine doubly shadowed craters within Haworth, Shoemaker, and Faustini using observations from the Dual frequency Synthetic Aperture Radar on Chandrayaan-2 reveals new constraints on the distribution of subsurface ice in the lunar South Polar region. We found only four craters, F2, F3, H3, and S1 that exhibit elevated CPR values (>1) within their interiors (Table 2), which is coupled with very low DOP values (<0.13), a refined diagnostic criterion for identifying volumetric scattering from subsurface. The lack of radar signatures indicative of volumetric scattering in the remaining craters potentially suggests that subsurface ice distribution within permanently shadowed regions is spatially heterogeneous. Moreover, the emplacement and retention of subsurface ice in individual craters might vary depending on the formation and evolutionary history of the craters, regolith properties, and the local geological setting. Hence, caution is warranted when generalizing these conclusions for larger perspectives. Among the studied craters, interior of crater F2 displays the strongest radar evidence, extensive CPR enhancement, low DOP, and a prominent lobate-rim morphology, suggesting excavation into subsurface ice within Faustini permanently shadowed region. The results validate that integrating radar based polarimetric diagnostics with morphology and thermal constraints provides a robust means of differentiating genuine ice-rich terrains from rough, rocky surfaces and point to a spatially heterogeneous distribution of subsurface ice at the lunar poles.

Methods

CPR and DOP calculations

In full polarimetric (FP) mode, transmission is in horizontal (H) and vertical (V) polarization, and reception is in all four combinations-HH, HV, VH, and VV. From the full polarimetric (FP) data, CPR image is derived using ref. 40, expressed in terms of HH and VV returns[39] as given below in Eq. 1:

$$\mathrm{CPR}(\mu_c) = \frac{\sigma^{\circ}_{HH} + \sigma^{\circ}_{VV} + 2\sqrt{\sigma^{\circ}_{HH}\sigma^{\circ}_{VV}}}{\sigma^{\circ}_{HH} + \sigma^{\circ}_{VV} - 2\sqrt{\sigma^{\circ}_{HH}\sigma^{\circ}_{VV}}} \quad (1)$$

It is an indicator of frozen volatile deposits[54] and is observed to be anomalously large ($CPR > 1$) for volume scattering from ice deposits[36], whereas, typically, regolith has $CPR < 1$[7].

$$\text{Degree of polarization (m)} = \frac{\sqrt{S_2^{\,2} + S_3^{\,2} + S_4^{\,2}}}{S_1} \quad (2)$$

In equation 2, S_1, S_2, S_3, S_4 are real numbers known as stokes parameters[54].

If low m then it is volume scattering, and if high m then it means double bounce scattering[32,55].

Data availability

Chandrayaan-2 Dual-Frequency Synthetic Aperture Radar calibrated data is available publicly at the Chandrayaan-2 portal of the ISRO Science Data Archive (ISDA) at https:/pradan.issdc.gov.in/ch2. The calibrated, map projected, ShadowCam data products are available publicly at https:/data.im-ldi.com/lunaserv.html.

Received: 4 February 2026; Accepted: 31 March 2026;
Published online: 06 May 2026

References

1. Watson, K., Murray, B. & Brown, H. On the possible presence of ice on the Moon. *J. Geophys. Res.* **66**, 1598–1600 (1961).
2. Arnold, J. R. Ice in the lunar polar regions. *J. Geophys. Res. Solid Earth* **84**, 5659–5668 (1979).
3. Feldman, W. C. et al. Fluxes of fast and epithermal neutrons from Lunar Prospector: Evidence for water ice at the lunar poles. *Science* **281**, 1496–1500 (1998).
4. Mitrofanov, I. G. et al. Hydrogen mapping of the lunar south pole using the LRO neutron detector experiment LEND. *Science* **330**, 483–486 (2010).
5. Lawrence, D. J. et al. Sensitivity of orbital neutron measurements to the thickness and abundance of surficial lunar water. *J. Geophys. Res. Planets* **116** (2011).
6. Gladstone, G. R. et al. Far-ultraviolet reflectance properties of the Moon's permanently shadowed regions. *J. Geophys. Res. Planets* **117** (2012).
7. Spudis, P. D. et al. Evidence for water ice on the Moon: results for anomalous polar craters from the LRO Mini-RF imaging radar. *J. Geophys. Res. Planets* **118**, 2016–2029 (2013).
8. Hayne, P. O. et al. Evidence for exposed water ice in the Moon's south polar regions from Lunar Reconnaissance Orbiter ultraviolet albedo and temperature measurements. *Icarus* **255**, 58–69 (2015).
9. Fisher, E. A. et al. Evidence for surface water ice in the lunar polar regions using reflectance measurements from the Lunar Orbiter Laser Altimeter and temperature measurements from the Diviner Lunar Radiometer Experiment. *Icarus* **292**, 74–85 (2017).
10. Sanin, A. B. et al. Hydrogen distribution in the lunar polar regions. *Icarus* **283**, 20–30 (2017).
11. Li, S. et al. Direct evidence of surface exposed water ice in the lunar polar regions. *Proc. Natl. Acad. Sci. USA* **115**, 8907–8912 (2018).
12. Putrevu, D. et al. Lunar impact craters: new perspectives from full-polarimetric analysis of Chandrayaan-2 dual-frequency SAR data. *J. Geophys. Res. Planets* **128**, e2023JE007745 (2023).
13. Shearer, C. K., Sharp, Z. D. & Stopar, J. Exploring, sampling, and interpreting lunar volatiles in polar cold traps. *Proc. Natl. Acad. Sci. USA* **121**, e2321071121 (2024).
14. Anand, M. et al. A brief review of chemical and mineralogical resources on the Moon and likely initial in situ resource utilization (ISRU) applications. *Planet. Space Sci.* **74**, 42–48 (2012).
15. Chakraborty, T., Syed, T. H., Heggy, E., Putrevu, D. & Dutta, U. On the reachability and genesis of water ice on the Moon. *ISPRS J. Photogramm. Remote Sens.* **211**, 392–405 (2024).

16. Zhang, J. L., Li, Y. Z. & Zhang, Y. A concise review of resource requirements for future space exploration. *Adv. Space Res.* **73**, 5363–5382 (2024).
17. O'Brien, P. & Byrne, S. Double shadows at the lunar poles. *Planet. Sci. J.* **3**, 258 (2022).
18. Carruba, V. & Coradini, A. Lunar cold traps: effects of double shielding. *Icarus* **142**, 402–413 (1999).
19. Sefton-Nash, E. et al. Evidence for ultra-cold traps and surface water ice in the lunar south polar crater Amundsen. *Icarus* **332**, 1–13 (2019).
20. Bussey, D. B. J. et al. Permanent shadow in simple craters near the lunar poles. *Geophys. Res. Lett*. **30** (2003).
21. Siegler, M., Paige, D., Williams, J. P. & Bills, B. Evolution of lunar polar ice stability. *Icarus* **255**, 78–87 (2015).
22. Mazarico, E., Neumann, G. A., Smith, D. E., Zuber, M. T. & Torrence, M. H. Illumination conditions of the lunar polar regions using LOLA topography. *Icarus* **211**, 1066–1081 (2011).
23. Paige, D. A. et al. Diviner lunar radiometer observations of cold traps in the Moon's south polar region. *Science* **330**, 479–482 (2010).
24. Williams, J. P. et al. Seasonal polar temperatures on the Moon. *J. Geophys. Res. Planets* **124**, 2505–2521 (2019).
25. Gibson, E. K. Jr. & Moore, G. W. Volatile-rich lunar soil: evidence of possible cometary impact. *Science* **179**, 69–71 (1973).
26. Mandt, K. E. et al. Exogenic origin for the volatiles sampled by the Lunar CRater observation and sensing satellite impact. *Nat. Commun.* **13**, 642 (2022).
27. Needham, D. H. & Kring, D. A. Lunar volcanism produced a transient atmosphere around the ancient Moon. *Earth Planet. Sci. Lett.* **478**, 175–178 (2017).
28. Zuber, M. T. et al. Constraints on the volatile distribution within Shackleton crater at the lunar south pole. *Nature* **486**, 378–381 (2012).
29. Qiao, L., Ling, Z., Head, J. W., Ivanov, M. A. & Liu, B. Analyses of Lunar Orbiter Laser Altimeter 1064-nm albedo in permanently shadowed regions of polar crater flat floors: Implications for surface water ice occurrence and future in situ exploration. *Earth Space Sci.* **6**, 467–488 (2019).
30. Colaprete, A. et al. Detection of water in the LCROSS ejecta plume. *Science* **330**, 463–468 (2010).
31. Schultz, P. H. et al. The LCROSS cratering experiment. *Science* **330**, 468–472 (2010).
32. Raney, R. K., Cahill, J. T., Patterson, G. W. & Bussey, D. B. J. The m-chi decomposition of hybrid dual-polarimetric radar data with application to lunar craters. *J. Geophys. Res. Planets* **117** (2012).
33. Thomson, B. J. et al. An upper limit for ice in Shackleton crater as revealed by LRO Mini-RF orbital radar. *Geophys. Res. Lett*. **39** (2012).
34. Campbell, B. A. High circular polarization ratios in radar scattering from geologic targets. *J. Geophys. Res. Planets*, **117** (2012).
35. Campbell, B. A. et al. Earth-based 12.6-cm wavelength radar mapping of the Moon: New views of impact melt distribution and mare physical properties. *Icarus* **208**, 565–573 (2010).
36. Spudis, P. D. et al. Initial results for the north pole of the Moon from Mini-SAR, Chandrayaan-1 mission. *Geophys. Res. Lett*. **37** (2010).
37. Patterson, G. W. et al. Bistatic radar observations of the Moon using Mini-RF on LRO and the Arecibo Observatory. *Icarus* **283**, 2–19 (2017).
38. Hapke, B. Coherent backscatter and the radar characteristics of outer planet satellites. *Icarus* **88**, 407–417 (1990).
39. Campbell, B. A. Radar remote sensing of planetary surfaces. (Cambridge University Press, 2002).
40. Mishchenko, M. I. The angular width of the coherent back-scatter opposition effect: an application to icy outer planet satellites. *Astrophys. Space Sci.* **194**, 327–333 (1992).
41. Peters, K. J. Coherent-backscatter effect: a vector formulation accounting for polarization and absorption effects and small or large scatterers. *Phys. Rev. B* **46**, 801 (1992).
42. Thompson, T. W., Ustinov, E. A. & Heggy, E. Modeling radar scattering from icy lunar regoliths at 13 cm and 4 cm wavelengths. Journal of Geophysical Research: Planets, 116 (2011).
43. Fa, W. & Eke, V. R. Unravelling the mystery of lunar anomalous craters using radar and infrared observations. *J. Geophys. Res. Planets* **123**, 2119–2137 (2018).
44. Bhiravarasu, S. S. et al. Chandrayaan-2 dual-frequency synthetic aperture radar (DFSAR): Performance characterization and initial results. *Planet. Sci. J.* **2**, 134 (2021).
45. Verma, N., Bhatt, M., Dangi, M., Kumar, S. & Bhardwaj, A. Exploring water-ice deposits in lunar polar craters with Chandrayaan-2 DFSAR data. *Icarus* **432**, 116492 (2025).
46. Robinson, M. S. et al. Seeing in the shadows. Lunar and Planetary Science Conference, LPI Contribution No. 3040, Id 1669, (2024).
47. Mandt, K. E. et al. LRO-LAMP detection of geologically young craters within lunar permanently shaded regions. *Icarus* **273**, 114–120 (2016).
48. Williams, J. P. et al. The Faustini permanently shadowed region on the moon. *Planet. Sci. J.* **5**, 209 (2024).
49. Basilevsky, AT., Krasilnikov, S. S. & Li, Y. Photogeological analysis of ShadowCam images of the permanently shadowed floor of lunar crater Shoemaker. *Planet. Space Sci.* **254**, 105998 (2024).
50. Neish, C. D. et al. Global distribution of lunar impact melt flows. *Icarus* **239**, 105–117 (2014).
51. Mishra, P., Kumar, S. & Singh, D. An approach for finding possible presence of water ice deposits on lunar craters using MiniSAR data. *IEEE J. Sel. Top. Appl. Earth Observ. Remote Sens.* **8**, 30–38 (2014).
52. Marco Figuera, R., Riedel, C., Rossi, A. P. & Unnithan, V. Depth to diameter analysis on small simple craters at the lunar south pole—possible implications for ice harboring. *Remote Sens.* **14**, 450 (2022).
53. Fassett, C. I. et al. Topographic diffusion revisited: Small crater lifetime on the Moon and implications for volatile exploration. *J. Geophys. Res. Planets* **127**, e2022JE007510 (2022).
54. Siegler, M., Keane, J. & Paige, D. Subsurface ice stability on the moon. *Lunar Polar Volatiles* **2087**, 5038 (2018).
55. Mohan, S., Das, A. & Chakraborty, M. Studies of polarimetric properties of lunar surface using mini-SAR data. *Curr. Sci.* **101**, 159–164 (2011).
56. Barker, M. K. et al. A new view of the lunar south pole from the lunar orbiter laser altimeter (LOLA). *Planet. Sci. J.* **4**, 183 (2023).

Acknowledgements

We are grateful and thank the Editor and both the reviewers for thorough assessment of our manuscript and for providing us constructive comments and suggestions. Department of Space, Government of India is thanked for supporting this study. The Chandrayaan-2 Dual Frequency Synthetic Aperture Radar experiment was designed and developed by Space Applications Centre, Ahmedabad (https://www.sac.gov.in/). We acknowledge the entire Chandrayaan-2 Dual Frequency Synthetic Aperture Radar team for their extensive support and contribution in successful planning, implementation, and acquisition of the Dual Frequency Synthetic Aperture Radar datasets. Indian Space Science Data Center (ISSDC) is acknowledged for archiving the Chandrayaan-2 Dual Frequency Synthetic Aperture Radar data for public access. ShadowCam is a NASA-funded instrument hosted onboard the Korea Aerospace Research Institute, Korea Pathfinder Lunar Orbiter satellite. We acknowledge the ShadowCam Science Operations Center, located at the Arizona State University in Tempe, AZ, for planning and executing instrument commanding, data processing and archiving imagery and associated data products. Geological samples are not used in the present study. This research received no external funding.

Author contributions

R.K.S. and R.R.B. led the conceptualization of the study and contributed to data analysis and scientific interpretation. K.A. analyzed the thermal environment of the craters, including temperature and crater formation related aspects. R.R.B., R.K.S., and S.K.M. investigated Circular

Polarization Ratio (CPR) based dielectric permittivity and subsurface material properties. R.K.S. and N.S. carried out crater morphological analyses using ShadowCam imagery. All authors (R.K.S., R.R.B., K.A., S.K.M., N.S., and A.B.) contributed to scientific discussions and to the preparation and revision of the manuscript. All authors have read and approved the manuscript.

Competing interests

The authors declare no competing interests.

Additional information

Supplementary information The online version contains supplementary material available at https://doi.org/10.1038/s44453-026-00038-9.

Correspondence and requests for materials should be addressed to Rishitosh K. Sinha.